

# In-beam PET and Compton imaging for enhanced accuracy proton-range verification

Javier Balibrea-Correa<sup>1,\*</sup>, Jorge Lerendegui-Marco<sup>1</sup>, Ion Ladarescu<sup>1</sup>, Carlos Guerrero<sup>2</sup>, Teresa Rodríguez-González<sup>2,3</sup>, Maria del Carmen Jiménez-Ramos<sup>3,4</sup>, Begoña Fernández-Martínez<sup>2,3</sup>, and César Domingo-Pardo<sup>1</sup>

<sup>1</sup>Instituto de Física Corpuscular, CSIC-University of Valencia, Valencia, Spain

<sup>2</sup>Dept. de Física Atómica, Molecular y Nuclear. Universidad de Sevilla, Seville, Spain.

<sup>3</sup>Centro Nacional de Aceleradores (Universidad de Sevilla-Junta de Andalucía-CSIC), Seville, 41092, Spain

<sup>4</sup>Department of Applied Physics II, ETSA, University of Seville, Seville, Spain

\*javier.balibrea@ific.uv.es

## ABSTRACT

We report on a combined in-beam PET and prompt-gamma Compton imaging system aimed at ion-range verification in proton-therapy treatments. A proof-of-concept experiment was carried out at the radiobiology beam line of the CNA cyclotron facility using a set of two synchronous Compton imagers and different target materials. The time structure of the 18 MeV proton beam was shaped with a series of beam-on and beam-off intervals, thereby mimicking a pulsed proton beam on a long time scale. During beam-on Compton imaging was performed utilizing the high energy  $\gamma$ -rays promptly emitted from the nuclear reactions in the target. In the course of the beam-off intervals in-situ positron-emission tomography was accomplished with the same imagers using the  $\beta^+$  decay of short-lived activated nuclei. The targets used were stacks of different materials covering also various proton ranges and energies. The experimental results obtained in this work are compared with a Monte Carlo model of the experimental setup. The results demonstrate the possibility to combine both imaging techniques in a concomitant way, where high-efficiency Compton imaging is complemented with the high spatial accuracy of PET. Empowered by these results we discuss a new methodology for enhanced accuracy and real-time ion-range monitoring. We suggest that a pulsed beam with a suitable duty cycle, in conjunction with in-situ Compton- and PET-imaging may help to attain both real-time and high-accuracy range monitoring.

## Introduction

Accurate ion-range determination is a key aspect in modern proton-therapy treatments<sup>1</sup>. This technique allows one to target very precisely the tumor area thanks to the large energy deposition at the end of the proton track (Bragg peak). As a consequence, hadron therapy minimizes damage in neighbouring tissues, thereby reducing also long term secondary effects. Hence, it is particularly well-suited for many pediatric cases and tumors close to sensitive organs<sup>1</sup>. However, the full potential of proton therapy is still hindered by the lack of high-accuracy real-time range verification, which would enable to use particle beams as a precise and non-invasive scalpel. This could extend the applicability of proton therapy also to diseases such as ventricular tachycardia and many other cardiovascular disorders<sup>2-4</sup>, thereby enlarging the number of patients benefiting from therapeutic high-energy beams.

As the incident proton beam slows down and stops inside the patient tissue, nuclear reactions take place all along the projectile path producing quasi-instantaneously (prompt) emission of secondary radiation<sup>5</sup>. This radiation, mainly  $\gamma$ -rays with energies spanning up to 5-6 MeV, are especially well suited to monitor the range of the ion beam. Prompt-Gamma (PG) monitoring has the advantage of the high spatial correlation with the primary ion range<sup>5</sup>. From a practical point of view, a major challenging aspect for real-time PG monitoring is the small signal-to-background ratio, which is commonly constrained by the limited efficiency of the detection apparatus, by the contaminant radiation arising from proton-beam interactions along different parts of the accelerator gantry, as well as by neutron contaminant reactions in the measuring instruments and in different parts of the surrounding area<sup>1,6</sup>.

In addition to PG monitoring there are other detection techniques for ion range verification, such as in-beam and off-beam PET imaging<sup>1,7</sup>. The latter is obviously not suited for real-time range assessment and in this work we discuss only the former. This methodology is based on the simultaneous detection of two 511 keV annihilation  $\gamma$ -rays coming from the  $\beta^+$  decay of short-lived nuclei activated by the hadron beam. The most abundant  $\beta^+$  emitters produced during the treatment are  $^{15}\text{O}$  and  $^{11}\text{C}$  with half-lives of 112 s and 20.4 m, respectively. The latter are mainly suited for a PET imaging control only after irradiation<sup>8-10</sup>.

Several configurations have been proposed for in-beam PET imaging starting from the simplest two detection systems working in time-coincidence to complex cylindrical ring configurations<sup>11,12</sup>. The latter have evolved toward a combination of PET and Compton imaging<sup>13,14</sup>, similar to the approach discussed in this work, but aimed at other clinical applications.

Our detection system is based on modular and high-efficiency Compton cameras, called i-TED<sup>15</sup>. The latter have been specifically designed for neutron-capture nuclear physics experiments using the Time-Of-Flight (TOF) technique<sup>16,17</sup>. In this type of experiments, the  $\gamma$ -ray yields from the  $(n, \gamma)$  reactions of interest are rather weak compared to the background arising from contaminant neutron interactions in different materials of the experimental area. Also, neutron capture  $\gamma$ -ray energies of interest typically span from hundreds of keV up to 5-6 MeV. Developments made to optimize the last two aspects in nuclear-physics experiments are also well suited for the implementation of i-TED in the present application. Thus, each i-TED module consists of two planes of Position Sensitive Detectors (PSD) and, aiming at maximizing detection efficiency, each PSD uses largest commercially available  $\text{LaCl}_3(\text{Ce})$  monolithic scintillation crystals with a size of  $50 \times 50 \text{ mm}^2$  optically coupled to  $8 \times 8$  pixels Silicon Photomultipliers (SensL ArrayJ-60035-65P-PCB). To enhance further the solid angle for Compton events each absorber plane consists of four, 25 mm thick, PSDs covering an area of  $100 \times 100 \text{ mm}^2$  in each i-TED module. For a point-like 1 MeV  $\gamma$ -ray source at 5 cm distance from the front face of the module, the coincidence detection efficiency is  $\sim 0.2\%$ . Regarding neutron-induced background suppression,  $\text{LaCl}_3(\text{Ce})$  ensures a small sensitivity to neutron interactions in the detection volume itself<sup>18</sup>, while offering also a large intrinsic detection efficiency. Finally, the high time-resolution obtained with the implemented acquisition system (PETsys Front-End Board D version 2 (FEB/D-1024)), with coincidence-time resolutions of  $\text{CTR} \sim 500 \text{ ps}$ , help to reduce random coincidences and other related backgrounds that could degrade the Compton imaging. For further details of the i-TED modules and developments on the  $\gamma$ -ray position reconstruction the reader is referred to<sup>15,19</sup>.

In this work we explore the applicability and performance of two i-TED modules working independently as PG Compton and in-beam PET imagers, using different time-coincidence strategies between the PSDs of the i-TED modules and a pulsed beam-time structure. A study of the performance of i-TED as Compton- and PET-imager is reported below in Methods, in section Laboratory characterization of the i-TED imaging system. The combined PG monitoring and in-beam PET experiment was carried out at the radiobiology beam line of the 18 MeV proton cyclotron facility at CNA<sup>20</sup> during two consecutive days. Radiobiological research using this type of low energy particle accelerators has attracted a lot of interest in the last decades concurring with the worldwide expansion of hadron-therapy centers<sup>21</sup>.

The cyclotron facility at CNA consists of a Cyclone 18/9 model equipped with an external beam line for multi-purpose research. The cyclotron accelerates protons and deuterons to 18 and 9 MeV, respectively. The beam is then delivered to the dedicated experimental area through a complex beam extraction system. For further details about the research beam line the reader is referred to<sup>22</sup>.

During the experiment, a 18 MeV proton beam was delivered to the experimental area with current values varying from 500 pA up to 1 nA on target, adding-up a total charge ranging from 212 to 674 nC per irradiation, depending on the total irradiation time and specific duty cycle used that will be explained later.

A picture of the experimental setup is displayed in Fig. 1. This configuration was chosen for a twofold study, on the one hand, to measure proton-induced  $\beta^+$ -emitter production cross sections<sup>23</sup> and, on the other hand, to explore the combination of Compton and PET imaging for ion-range verification, which is the main objective of this article. The proton beam direction is indicated by the red arrow. A sample holder (elongated U-shaped piece in the center) was used to simultaneously expose regularly spaced thin sample-foils to the proton-beam. Both the holder and the samples themselves were specifically designed for a parallel study devoted to the determination of production cross sections of  $\beta^+$  emitting isotopes<sup>23,24</sup>. However, as discussed later, this set-up turned out to be very well suited for the simultaneous demonstration of PET and Compton imaging discussed in this work. The holder was aligned with the proton beam axis, thereby inducing a similar irradiation field for all samples under study. The material of the samples holder was polylactic acid (PLA) plastic with a size of  $5.2 \times 5.5 \times 10.3 \text{ cm}^3$ . The central hole had a size of  $3.2 \times 4.12 \text{ cm}^2$ . The target samples consisted of thin layers of different materials (described below), which were placed using five dedicated slots with a regular gap of 1.6 cm. The samples consisted of thin square layers with dimensions of  $41.2 \times 41.2 \times 0.8 \text{ mm}^3$ , fitting into the dedicated slots of the holder. Two different materials were used, Nylon and PMMA, with nominal densities of 1.15 and 1.18  $\text{g/cm}^3$ , respectively. At the very end of the samples holder a 2 mm thick graphite layer was added, with the twofold purpose of fully stopping the proton beam and registering the proton-current values during the experiment.

The holder-samples assembly was supplemented with an additional PLA matrix, which is also shown in Fig 1. This PLA matrix was remotely controlled and designed to fill the gap between the samples after each proton-beam irradiation, thereby acting as  $\beta^+$  converter and lowering the spatial range of the  $\beta^+$  particles when inserted. Fig. 2 shows a schematic drawing of the moderator-converter assembly, which can help to get a better understanding of this set-up.

The two i-TED modules used during the experiment were placed front-to-front on both sides of the proton beam axis, fully covering the in-beam PET field of view of the samples under study. The i-TED module labelled as i-TED-A used an aluminum



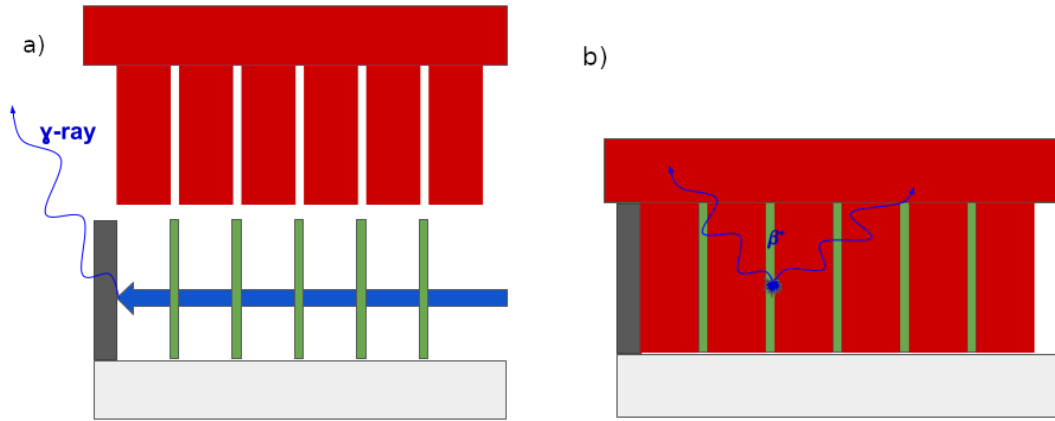


**Figure 2.** Schematic drawing of the experimental setup during the different part of the duty cycles. The thin layers under study are represented by green color, the thick graphite layer by gray and the PLA matrix by piece. Panel (a) shows the experimental setup during the beam-on period. In panel (b) is displayed the experimental setup during the beam-off period.

of clarity, in the following sections we refer to those configurations as the following:

- Configuration (I): Five Nylon layers and one thick graphite beam stopper.
- Configuration (II) Five Nylon layers and a graphite proton-beam energy degrader just before the Nylon samples.
- Configuration (III) Five PMMA layers and one thick graphite beam stopper.

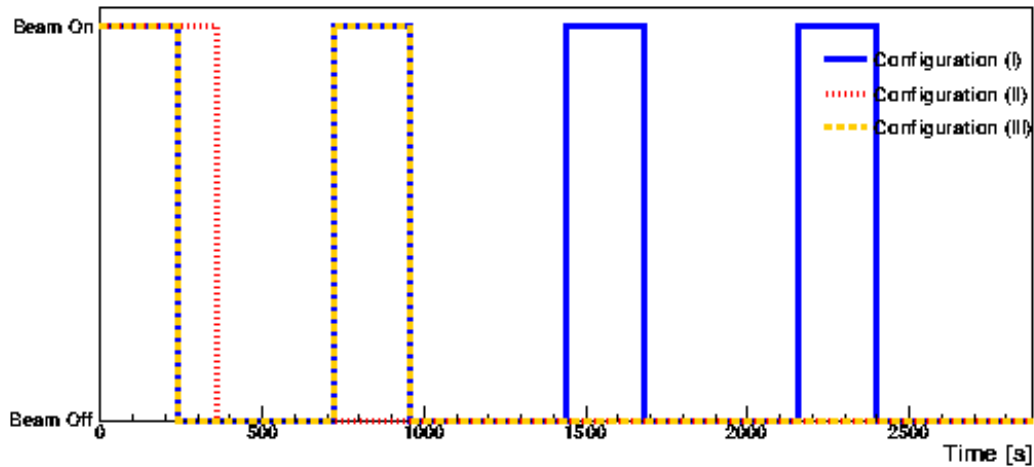


**Figure 3.** Schematic drawing of the experiment time structure used for the individual configurations used during the experiment. See text for details.

The time structure of beam-on and beam-off periods for each individual configuration are presented schematically by different colors in Fig. 3. In the case of configuration (I), there was four duty cycles of 240 s beam-on followed by 480 s of beam-off as displayed by blue-solid line. Configuration (II) consisted in one long irradiation of 360 s followed by a long time period of beam-off as the red-dashed line shown. At last, for configuration (III), it was made of 2 beam-on periods of 240 s time-spaced by 480 s followed by a long period of beam-off as the dashed-orange line represents.

The data reduction applied to the experimental data for the analysis of all the configurations is described below in the Data reduction section in Methods.

## Results

In the following sections we show the results obtained for each one of the configurations listed above.

### Results for Configuration (I)

The configuration (I) consisted of five Nylon layers and a thick graphite layer at the end of the stack of samples. This section presents the results obtained for Compton- and PET-imaging in the beam-on and beam-off modes, respectively.

#### *Compton imaging in the beam-on lapses*

The Compton images reconstructed from the experimental data acquired with i-TED-A and i-TED-B during the beam-on lapses of configuration (I) are displayed in panels (a) and (b) of Fig 4. Panels (c) and (d) show the reconstructed MC images for i-TED-A and i-TED-B, respectively.

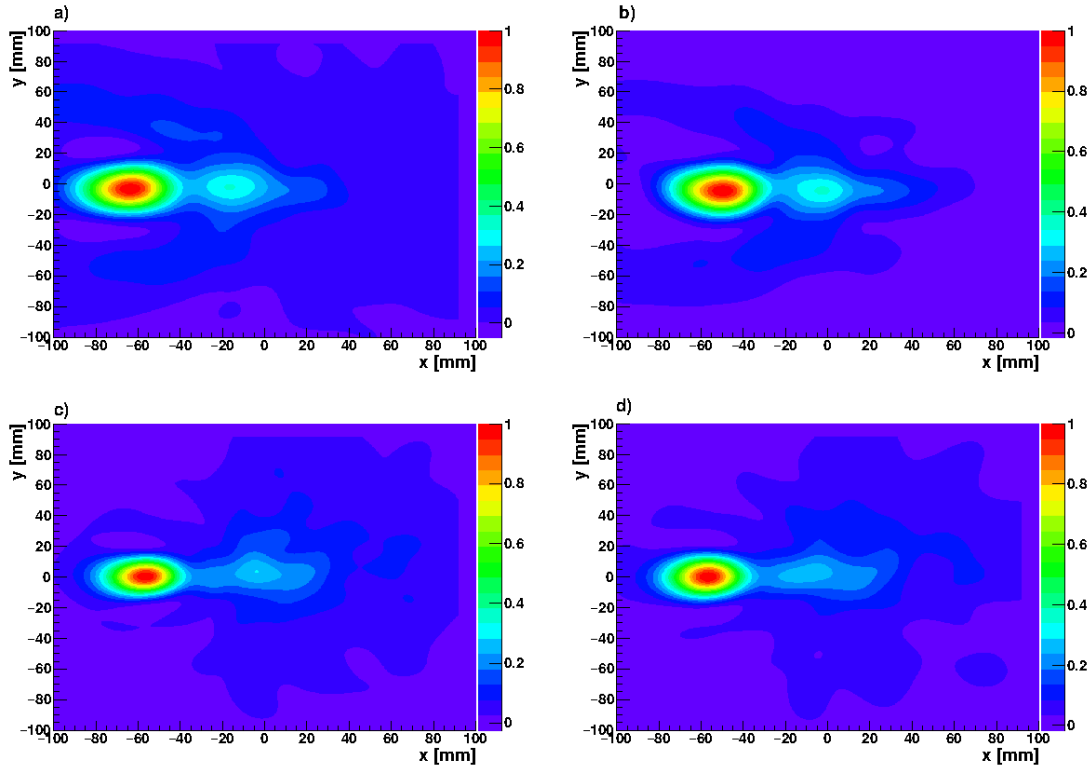


**Figure 4.** Reconstructed experimental and MC Compton images from PG  $\gamma$ -rays in configuration (I). See text for details.

The imaging reconstruction methodology is described below in the Methods section. As it can be observed in panels (a) and (b) of Fig. 4 the reconstructed experimental images for this configuration show a prominent maximum, which can be ascribed to prompt gamma-rays emitted from the thick graphite layer at the Bragg peak. A secondary maximum can be appreciated at the center of the image, corresponding to the geometrical center of the setup where detection efficiency is largest. The strength of these maxima depends on the different amount of material in each layer and the inelastic proton cross-section as a function of the proton energy. The fact that only the signature of the central Nylon layer can be observed indicates that detection efficiency and sensitivity are not enough to visualize the other four thin Nylon layers, as was to expect from the reduced thickness ( $800\mu\text{m}$ ). This statement is confirmed with the MC simulations. The MC images were reconstructed as the weighted superposition of the reconstructed MC images from the individual layers. The weighting values for each layer were calculated according to the amount of inelastic reactions with  $\gamma$ -rays spanning from 4 to 5 MeV registered at the individual layer in the dedicated proton MC simulation of this configuration.

The MC reconstructed images have a similar structure as the experimental ones, with a strong maximum at the graphite thick layer position and a second maximum in the central region of the image. If one compares the ratio between maxima in the experimental and MC images, the ratio changes from  $\sim 0.45$  down to  $\sim 0.35$ , respectively. This difference could be due to discrepancies between the evaluated cross-sections and/or stopping power present in the libraries (and hence on the MC results) and the actual real cross-section values.



### PET imaging in the beam-off lapses

The 2D PET image reconstructed from the experimental data of i-TED-A and i-TED-B during the beam-off intervals for configuration (I) is displayed in panel (a) of Fig. 5. The five irradiated layers can be clearly observed, well resolved from each other. The maxima are well correlate with the position of the irradiated layers, as it is discussed below.

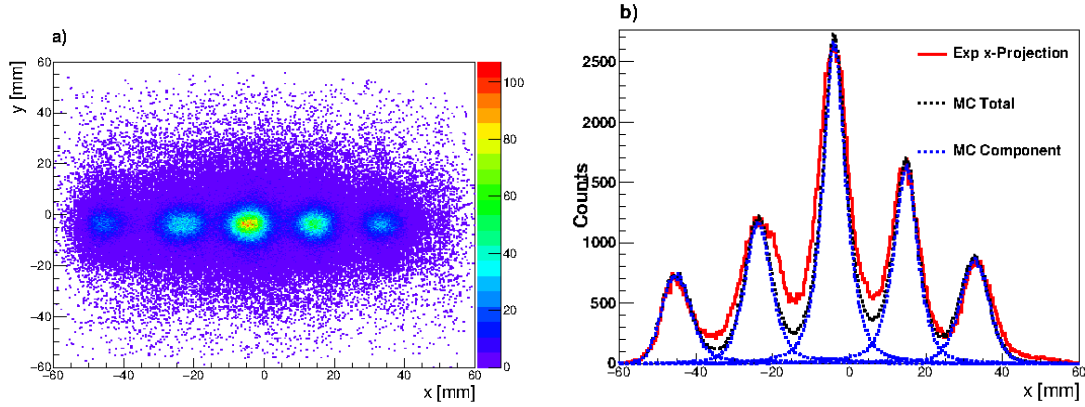


**Figure 5.** In panel (a), experimental 2D PET image for Configuration (I). Panel (b) 1D PET image x-projection (red) together with the Monte Carlo simulations of the individual contributions (blue) and total (black).

Panel (b) of Fig. 5 shows the x-axis projection of the experimental image (red) together with a MC simulation of the  $\beta^+$  emission of the activated layers (black). The MC image was reconstructed by weighting the PET images obtained from the simulation of the individual layers. The contribution of each layer is represented in Fig. 5 by a dashed-blue line. The spatial distribution used for the MC calculation is described in the Methods section below. The weight of each individual contribution was chosen to match the height of the reconstructed experimental distribution.

While the experimental distributions for the first, second and last sample slots are relatively well reproduced by the MC simulations, the third and fourth distribution positions are slightly broader than those reconstructed from the MC calculations. A plausible explanation for this effect might be that the PLA matrix did not fit these two layers perfectly, and thus the mean free path of the  $\beta^+$  particles coming out from those irradiated layers was larger, thus leading to an additional broadening of the measured distributions at those locations.

Tab. 1 shows the results obtained from a Gaussian fit of the experimental x-axis distribution of this configuration. The first column indicates the Nylon sample position. The second and third columns show the peak positions and widths ( $\sigma$ ). The last column contains the widths ( $\sigma$ ) from a Gaussian fit of the MC distribution at the corresponding positions.

Nylon sample	x [mm]	$\Delta x$ [mm]	$\sigma_{Exp}$ [mm]	$\sigma_{MC}$ [mm]
1	33.46(4)	-0.46(4)	4.16(4)	4.22
2	14.33(3)	0.67(3)	4.41(3)	4.03
3	-4.06(2)	-0.06(2)	4.22(2)	3.94
4	-23.11(3)	-0.89(3)	5.53(4)	4.17
5	-45.29(6)	-0.71(6)	4.07(7)	3.99

**Table 1.** Experimental Gaussian fit of the PET x-projection for configuration (I). The last column shows the widths obtained from the MC distributions.

These results thus confirm an overall fair agreement between simulation and experiment. It is worth to highlight the complementary performance of Compton and PET imaging in terms of detection sensitivity and spatial resolution, which indicates that a smart combination of both approaches in a convenient beam-time structure can result in an overall improvement of the ion-range assessment.

### Results for Configuration (II)

In this section we describe the results for the configuration (II), corresponding to five Nylon layers and a proton-beam energy degrader placed just before the samples holder. This is an interesting configuration because of the low beam energy (17 MeV at the first Nylon layer).

### Compton imaging in the beam-on lapses

The experimental reconstructed Compton images for i-TED-A and i-TED-B modules obtained for the configuration (II) are displayed in panels (a) and (b) of Fig 6. In the same figure, panels (c) and (d) shown the reconstructed MC images for i-TED-A and i-TED-B, respectively. Both, experimental and MC images were reconstructed following the same procedure described in the previous section.

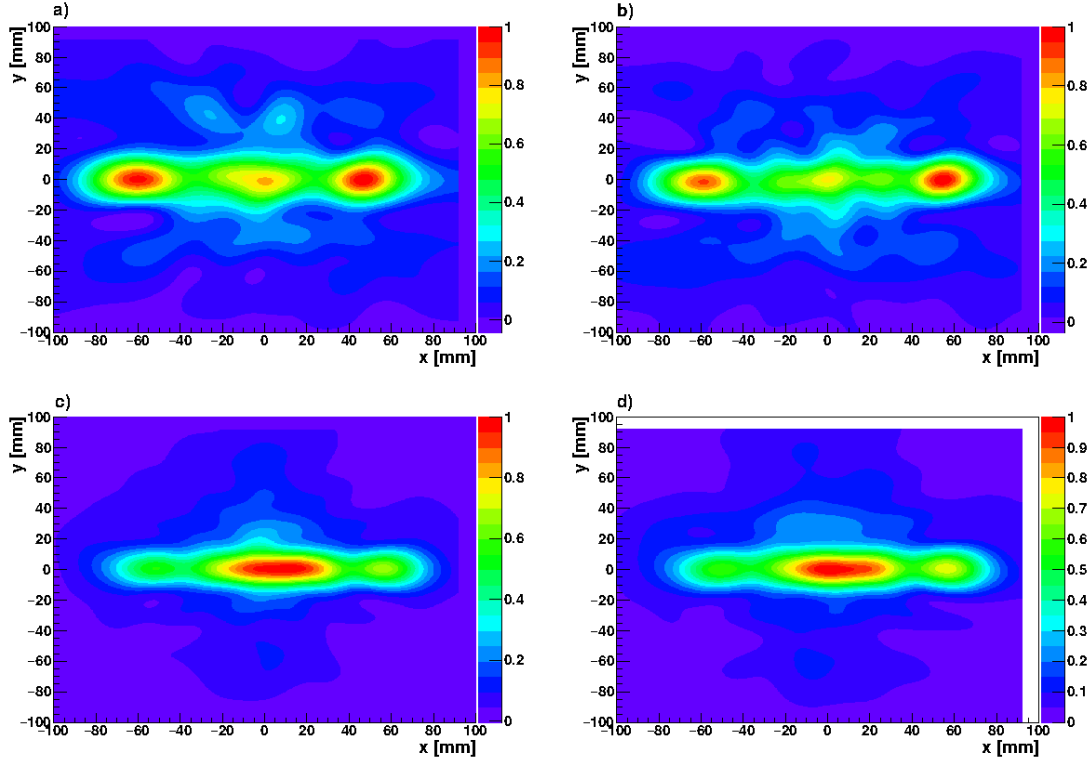


**Figure 6.** Compton images from PG  $\gamma$ -rays in configuration (II). See text for details.

For this specific configuration the experimental images of both i-TED modules show two intense emission maxima, with comparable strengths, at both extreme x-positions of the field of view. The first maximum on positive x-values agrees well with the location of the graphite degrader. The second maximum on the left-hand side (negative x-values), is situated at the same position of configuration (I), which is therefore consistent with the position of the thick graphite layer or beam stopper. In addition, in the center of the image one can appreciate another maximum, with an strength that is  $\sim 20\%$  lower than the two main lateral peaks.

Interestingly, in this configuration the reconstructed MC images do not reflect what is observed experimentally. The images, for both i-TED modules show a maximum in the central part of the image, where the Compton detection efficiency is maximum. It is worth to mention that between the central part and the positions where the thick graphite stopper and degrader are placed there is a difference of about  $\sim 30\%$ . Almost the same value but in the opposite direction compared to the experimental images. At this moment we can only ascribe this notable discrepancy to possible defficiencies in the cross-sections present in the evaluated libraries, especially at low proton energies.

### PET imaging in the beam-off lapses

The reconstructed experimental 2D PET image from the beam-off intervals of configuration (II) is displayed in panel (a) of Fig. 7. As for the case of the beam-on results, the obtained images are really interesting; In addition to the five Nylon layers, the  $\beta^+$  annihilation events at the entrance energy degrader is well observed at the right-hand side of the image ( $x=58$  mm), a position which is close to the edge of the PET field of view between both i-TED modules.

Panel (b) of Fig. 6 shows the x-axis projection of the experimental 2D PET image (red) and the MC simulation of the irradiated layers (black), in a similar fashion as it was made for configuration (I). The contribution of the individual layers is displayed in the same figure by a dashed-blue line. The MC distribution was also scaled to match the experimental distribution. The position of the layers in the geometry of the MC simulations was set to the same position of configuration (I). Actually, the the first and the last layer positions are reconstructed in the same position as configuration (I), a situation which does not

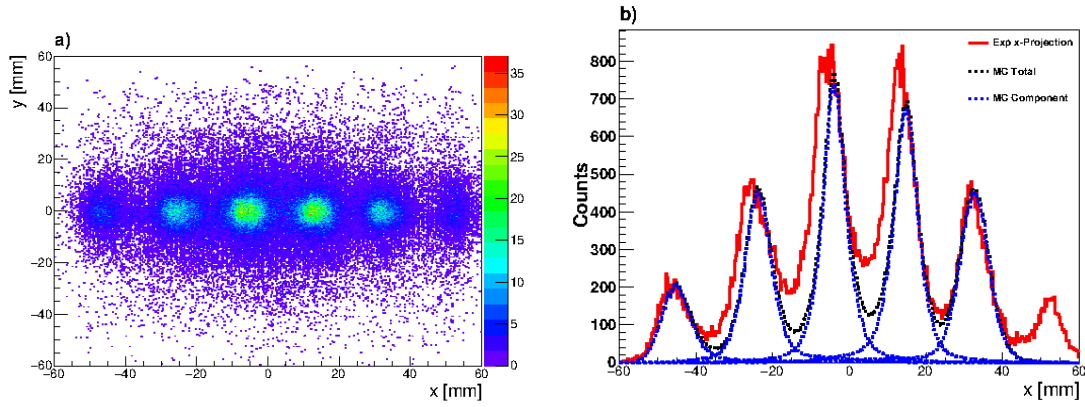


**Figure 7.** Experimental 2D PET image for Configuration II (a). PET image x-projection (red) together with the MC simulations of the individual images (blue) and the total MC distribution (black) are shown in panel (b).

occur for the second, third and fourth layers. This change may indicate a small displacement in experimental setup during the exchange of the irradiated layers. Also a small change in the direction of the proton beam after restarting the cyclotron irradiation should not be rejected.

As it was found for configuration (I), the obtained experimental width of the individual layers compared to the MC distributions seems to be larger (in average by 15%) for layer positions two, three and four.

The experimental distributions were fitted to Gaussian functions. The reconstructed position and widths ( $\sigma$ ), together with the MC widths are presented in Tab. 2.

Nylon sample	x [mm]	$\Delta x$ [mm]	$\sigma_{Exp}$ [mm]	$\sigma_{MC}$ [mm]
1	32.28(5)	0.72(5)	4.19(5)	4.23
2	13.15(4)	1.85(4)	4.4(4)	4.040
3	-5.35(4)	1.35(4)	4.57(5)	3.95
4	-24.71(5)	0.71(5)	5.02(6)	4.17
5	-46.5(2)	0.5(2)	4.1(2)	4.0

**Table 2.** Position and widths obtained by fitting a Gaussian function to the PET x-projections in configuration (II). The last column shows the width values obtained for the MC simulations.

Comparing the results of Tab. 2 with those obtained for configuration (I) in Tab. 1, the position of the second, third and fourth layers show a change of  $\sim 1$ mm, thus reflecting the good sensitivity of the PET imaging to the details of the experimental setup. As expected from the panel (b) of Fig. 7, the experimental and MC widths for the first and last layer are in good agreement, while for the second, third and fourth layer the experimental values are larger by 15%.

### Results for Configuration (III)

This section presents the results for the last set-up, configuration (III), corresponding with the irradiation of five PMMA layers. In this case no beam energy degrader was placed between the entrance window of the cyclotron and the samples holder.

#### Compton imaging in the beam-on lapses

The reconstructed experimental Compton images from prompt  $\gamma$ -rays for i-TED-A and i-TED-B during the beam-on intervals of configuration (III) are displayed in panels (a) and (b) of Fig 8. Panels (c) and (d) show the reconstructed MC images for the same modules.

As for configuration (I), the experimental Compton images reconstructed for both i-TED modules exhibit a main peak located at the position of the thick graphite layer and a second (smaller) maximum close the geometrical center of the experimental setup, in agreement with the location of the maximum Compton detection efficiency.

The reconstructed MC images, calculated in the same way as for previous configurations (I) and (II), show the strong emission peak at the thick graphite beam stopper. The secondary peak shows a double-peak structure that the experimental image does not have. In terms of relative intensities of the main and secondary peaks, the agreement between experiment and simulation is satisfactory. The ratio of intensities ranges from  $\sim 0.3$  for the experimental image to  $\sim 0.25$  for the MC.



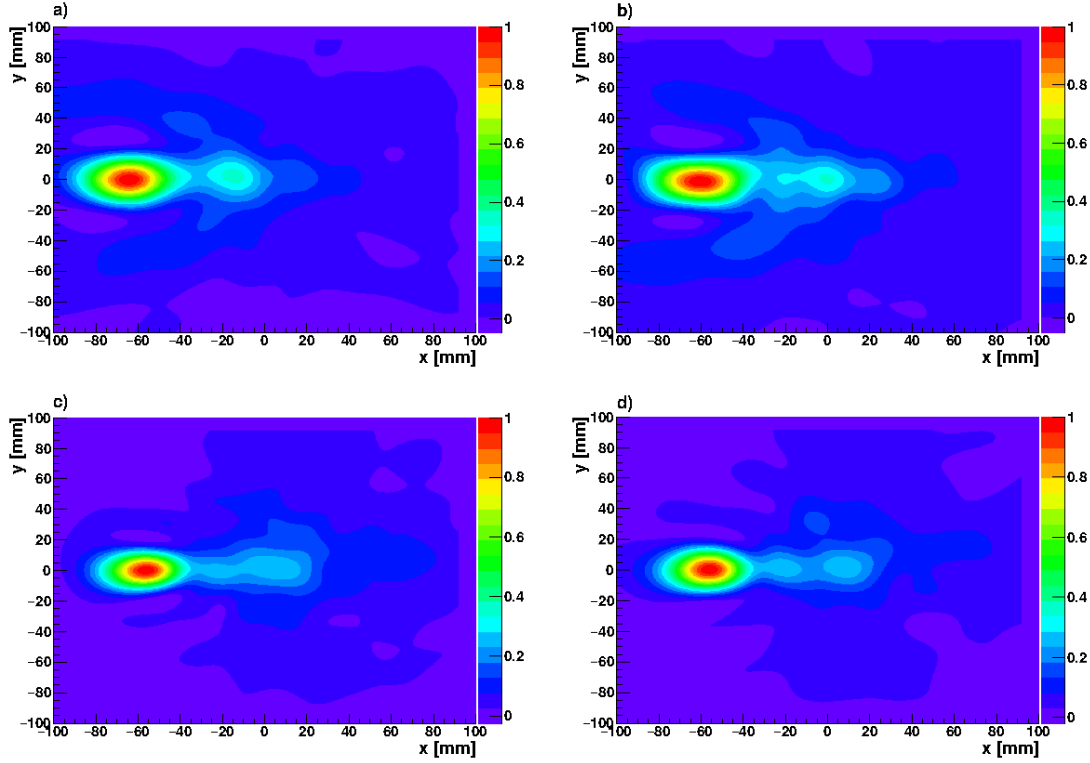


**Figure 8.** Compton images in configuration (III). See text for details.

### *PET imaging in the beam-off lapses*

The reconstructed experimental 2D PET image for this configuration during the beam-off period is displayed in panel (a) of Fig. 9. As for the previous configurations, the five layers can be clearly resolved and located at the true positions, thus demonstrating the fidelity of the PET imaging of the experimental setup for this type of measurements.

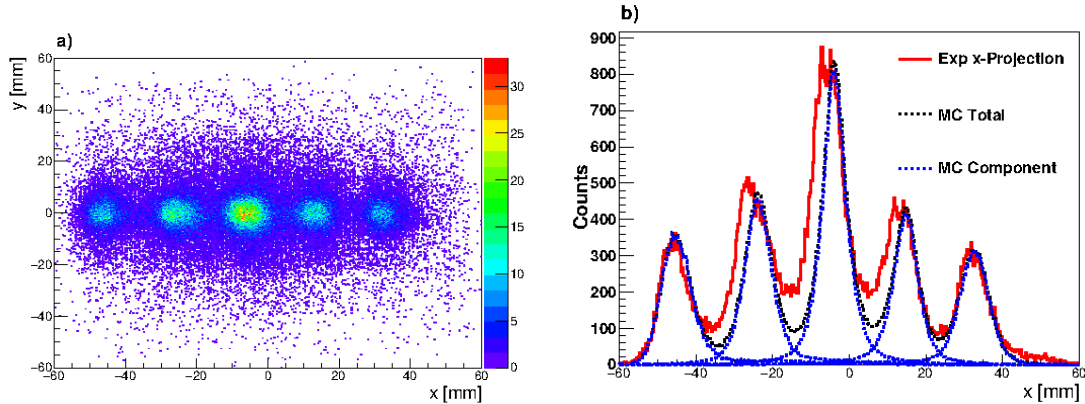


**Figure 9.** Experimental 2D PET image for Configuration (III) is shown in panel a). Panel b) shows the 1D PET image x-projection (red) together with the Monte Carlo simulations of the individual images (blue) and the total (black).

Panel (b) of the same figure shows the experimental PET x-axis projection (red) together with a MC simulation of the of the activated layers (black), in a similar way as it was calculated for the rest of configurations. The MC distributions, as in the previous sections, were also scaled to match with the height the experimental data, keeping the same positions as configuration (I).

The x-axis projections show that the results for this configuration have the same pattern than configurations (I) and (II).

The MC distribution matches very well the first and the last irradiated layers, while the experimental data of the central layers are broader and moved from what is expected from the MC simulations. The apparent position of the layers has the same displacement as in configuration (II) respect to (I), 1 mm. The fact that configuration (II) and (III) were performed one after the other in the second day of the experimental campaign could support the possibility that the proton beam was not impinging in the same exact position as for configuration (I).

Gaussian fits were performed for the x-axis distribution and the results are presented in Tab. 3

PMMA sample	x [mm]	$\Delta x$ [mm]	$\sigma_{Exp}$ [mm]	$\sigma_{MC}$ [mm]
1	32.34(5)	0.66(5)	4.09(6)	4.22
2	12.82(5)	2.18(5)	4.76(6)	4.03
3	-5.67(3)	1.67(5)	4.39(4)	3.91
4	-24.93(5)	0.94(5)	5.20(6)	4.15
5	-46.1(1)	0.1(1)	4.0(1)	4.0

**Table 3.** Positions and widths ( $\sigma$ ) obtained for the experimental PET x-projection for configuration (III). The last column shows the values obtained for the MC simulations.

The same pattern is observed for this configuration regarding the width of the distributions. The first and the last irradiated layers agree very well with each other. For the rest of layers the experimental width is slightly broader. This fact may again support the hypothesis that the PLA matrix did not fill completely the gaps of the central layers in the sample holder.

## Discussion and Conclusion

In this work we have demonstrated the possibility to use modular Compton cameras in a front-to-front and synchronous configuration in conjunction with a pulsed proton beam to perform quasi-simultaneous in-beam PET and prompt gamma-ray Compton imaging. This pilot experiment comprised a variety of materials and configurations, thereby aiming at addressing the systematic spatial uncertainties related to each one of the imaging techniques.

The PET spatial resolution obtained in this study is reported in Tab. 6 of the Methods section. The resolution is in agreement with the one calculated by means of MC simulations using individual crystal position reconstructions reported in a previous work<sup>19</sup>, and in line with similar pre-clinical PET-imaging prototypes (5-6 mm) reported in<sup>7</sup> and references therein. The repeatability performance of our PET system is given by the  $\Delta x$  differences between measured maxima and reference MC values for the target layers, as reported in tables 1, 2 and 3. Maximum deviations of about 2 mm were found, with average deviations typically within  $\sim 1$  mm or less. It is worth to mention that, at variance with our detection set-up, other PET works use smaller and thinner scintillation crystals, where pin-cushion and non-linearity effects are less severe<sup>19</sup>. However, a high efficiency is required when aiming at online monitoring, and also thick scintillation crystals are required to image high-energy prompt gamma-rays. The virtue of PET for ion-range monitoring is the attainable spatial sensitivity, resolution and repeatability. However, these advantages are shadowed by the fact that it can be hardly accomplished during beam irradiation and it requires also of a certain beam-off time-lapse for the  $\beta^+$  emitters to decay and acquire sufficient counting statistics. The latter drawbacks directly affect the total treatment time and increase the blurring due to wash-out effects.

The experimental PG Compton images were compared with the MC simulations of the different configurations and the single graphite layer in Fig. 4, 6, 8 and later in Fig. 17 of the Methods section. The image resolutions between both experimental and MC results are comparable, thus yielding an average spatial resolution of about 24 mm for both imagers. Small discrepancies observed during the irradiations between main and secondary peaks may point to deficiencies in nuclear cross-section data included in the evaluated libraries commonly used for MC simulations. This result for the spatial resolution cannot be directly compared with other works, as it strongly depends on the geometry of the set-up and the distance to the object under study. The repeatability of the reconstructed Compton images can be estimated from the position of the maximum for each imager and configuration (table 4). Deviations of 2 mm were found, with an average value of about 1 mm, which is slightly worse than that obtained with PET. However, deviations of almost 8 mm are found for the Compton reconstructed positions of the configuration II, when compared to the other two configurations. This effect is not fully understood yet, but it may indicate that the repeatability of the Compton reconstruction is more sensitive than PET to variations in beam energy or other experimental effects. On average, both resolution and repeatability are better in PET than in Compton imaging. Rather than the angular or spatial resolution itself, it is the sensitivity of the imaging apparatus to range shifts or variations what matters when it comes to addressing range verification<sup>18</sup>. The latter is more related to repeatability than resolution, although a higher image resolution is expected to deliver also a more reliable range monitoring. Still, one of the main advantages of Compton imaging is its suitability to carry out range verification in-situ and in real-time. From our pilot experiment the real-time capability of each imaging approach can be inferred from the average count rates in- and off-spill for each sub-system. These values are reported

i-TED	Configuration Max. Position in Compton (mm)		
	(I)	(II)	(III)
A	-71.17	-63.50	-70.50
B	-68.8	-64.16	-71.16
$\Delta x$	2.3	0.66	0.66

**Table 4.** Maximum emission position for Compton imaging (in mm) in the three configurations and both i-TED modules. The bottom line shows the differences between maxima, which reflect the repeatability of the measurement.

below in table 5. On average, a factor 300 higher counting rate is registered in-spill for Compton imaging, when compared to

	Configuration Avg. Count Rate (Counts/s)		
	(I)	(II)	(III)
Compton in-spill	13324	6642	14975
PET off-spill	61	29	20

**Table 5.** Average count rates for Compton imaging in-spill and for PET imaging off-spill.

off-spill with the PET technique. Therefore, to achieve a similar statistical accuracy with both imaging methods, a pulsed beam with a duty-cycle of 0.01, or smaller, becomes convenient.

In summary, to a large extent both PET and PG Compton are rather complementary approaches and may be used in a synergic fashion. Therefore, the possibility to combine them in a single and dedicated system, similar to the one reported here, seems a reasonable step forward towards attaining high accuracy range verification (PET) in real-time (Compton). In this respect, one of the main limitations of the present work was the low beam energy (18 MeV), when compared to clinical values (100-200 MeV). For this reason the beam on/off lapses used in this work had to be significantly large, of several 100 s and a special target or phantom had to be employed. Next steps to develop further the approach proposed here comprise the realization of measurements using average clinical beam conditions and conventional water or PMMA phantoms. Using a pulsed beam of a high energy with a large phantom and a suitable duty cycle, it may become possible to correlate sequential PG-Compton and PET-images in- and off-spill, respectively. There are two main aspects to research in the future experiment. First, the performance of the detection system at the high counting rate conditions of the high-energy and high-intensity clinical beams needs to be validated. Second, one has to determine which is the optimal duty-cycle for the proton beam to accomplish both PG Compton and PET imaging for a proper trade-off of statistical and systematic accuracy. The aforesaid pulsed-beam duty-cycle requirement of less than 0.01 aligns very well with the application of this new methodology in treatments with superconducting synchrocyclotrons, which produce a pulsed beam (few  $\mu$ s, every 1–2 ms)<sup>26</sup>, and also with recent developments related to hybrid delivery approaches in flash therapy<sup>27</sup>.

## Methods

### Data reduction

The individual detectors of each i-TED module were calibrated in energy using a point-like  $^{152}\text{Eu}$   $\gamma$ -ray source. In addition to the  $\gamma$ -ray lines corresponding to the strongest nuclear reactions identified during the proton irradiations at CNA were included in the energy calibration. The latter correspond to the  $^{12}\text{C}(p,p'\gamma)^{12}\text{C}$  and  $^{16}\text{O}(p,x\gamma)^{12}\text{C}$  nuclear reactions, both emitting 4.4 MeV  $\gamma$ -quanta<sup>6</sup>. The corresponding first and second escape peaks were also clearly visible and included in the calibration, as well as the 511 keV  $\gamma$ -ray from the detection of  $\beta^+$  annihilation events during the beam-on periods. A third polynomial degree was used to model the energy-ADC relation over this large energy range. An example of the individual energy calibration is displayed in Fig. 10. The experimental ADC values for the different  $\gamma$ -ray transitions are represented by red markers, while the fitted polynomial is displayed by the dashed-blue line.

The energy detection thresholds obtained for i-TED-A and i-TED-B were of 100 keV to 250 keV, respectively. The  $\gamma$ -ray interaction positions in the individual PSDs were reconstructed following the procedure described in<sup>19</sup>. The absolute  $\gamma$ -ray position interaction was obtained from the reconstructed intrinsic 3D position coordinates and the location of each PSD, which was well known by set-up construction.

The i-TED energy-calibrated add-back time-coincidence spectra between detection planes registered during the beam-on period of configuration (I) is displayed in Fig. 11. The spectra of i-TED-A and i-TED-B are represented by the blue and red lines, respectively. The time-coincidence window between different detection planes is 10 ns, which allowed to reduce random coincidences with other background sources. The deposited energy spectra registered during the three different configurations

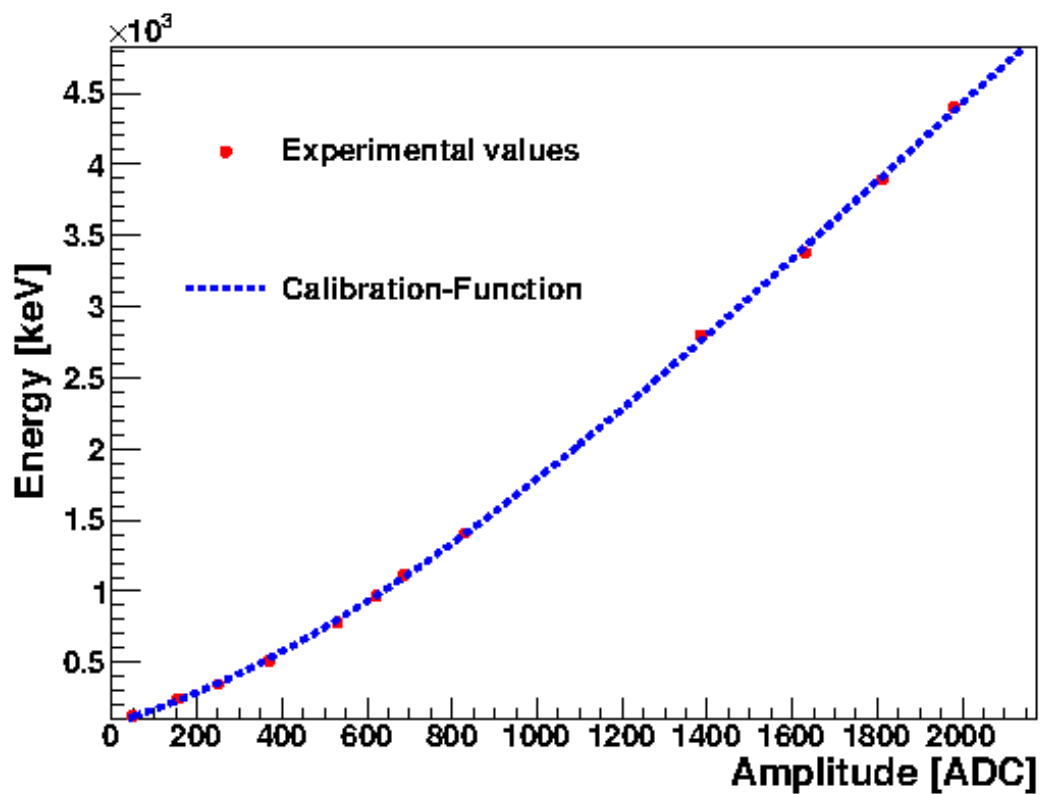


**Figure 10.** Energy calibration for an individual detector of i-TED-A. The experimental data from the  $^{152}\text{Eu}$  calibration source and  $\gamma$ -ray lines PG identified during beam-on periods are represented by the red dot points. The fitted third degree polynomial is plotted by the dashed blue line.

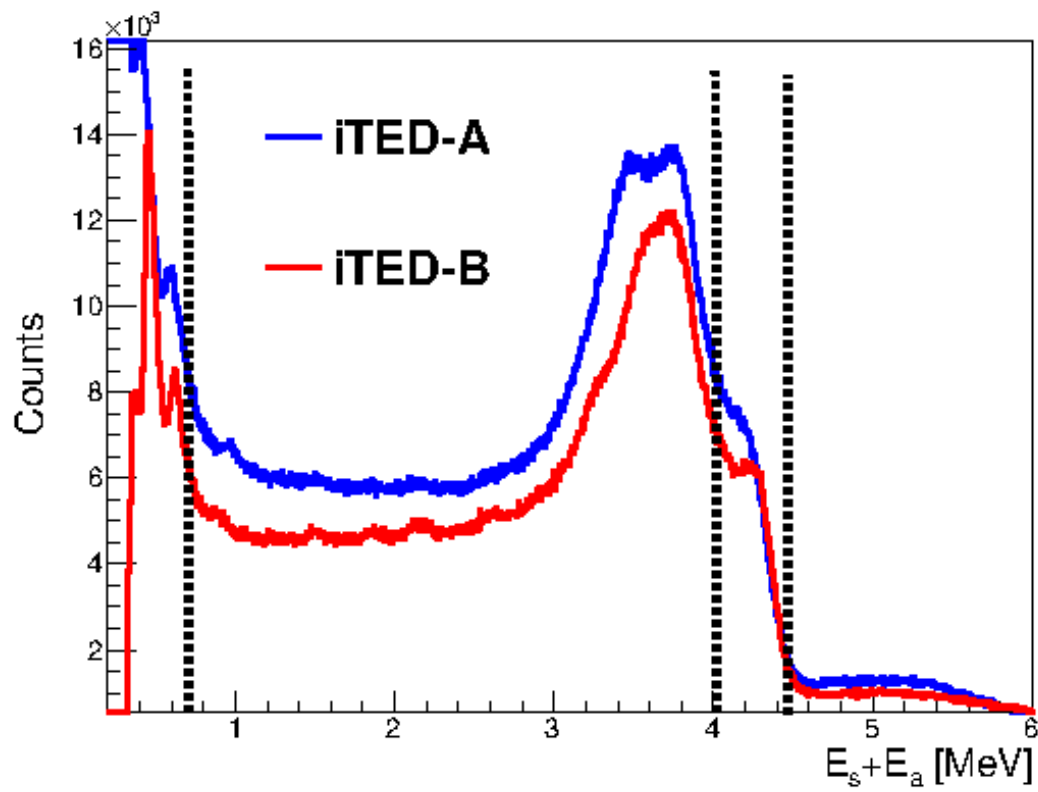


**Figure 11.** Add-back deposited energy detected by i-TED-A (blue) and i-TED-B (red) during the beam-on period. The dashed lines correspond to the energy threshold for imaging and the 4.4 MeV  $\gamma$ -ray line used for Compton imaging.



were similar in size and shape. This result might indicate the registered spectra are dominated by the inelastic reactions in Carbon isotopes at the thick graphite layer, an effect which is expected from the Bragg curve<sup>2,5</sup> and the large amount of material of the thick graphite target when compared to the thin samples of Nylon and PMMA.

The energy window of 4.0-to-4.6 MeV chosen for the beam-on periods to perform Compton imaging is displayed by dashed lines in Fig. 11. A high energy threshold for the individual absorber PSD detectors, 700 keV, was used for the Compton imaging reconstruction aiming at reducing artifacts in the images due to time-correlated pair production events and random coincidences with 511 keV. The image plane chosen for the Compton reconstruction corresponds to the axial direction of the samples holder, i. e. 8.5 cm from the frontal face of the i-TED-A module. Finally, the Compton images in this work were obtained by implementing the analytical inversion algorithm based on spherical harmonics developed by Tomotani and Hisarawa in 2002<sup>28</sup>. This inversion formula, which is based on an infinite Legendre polynomial expansion, leads to an approximate solution given by a unit vector in the image space,  $\vec{s}$ . The image at that vector position is described by

$$f(\vec{s}) \approx \int_{\cos\omega_{min}}^{\cos\omega_{max}} d\cos\omega \int_S d\vec{r} k^{-1}(\vec{r}, \vec{p}; \cos\omega) g(\vec{r}; \cos\omega), \quad (1)$$

where  $\vec{r}$  is a unit vector into the projection space,  $\omega_{min}$  and  $\omega_{max}$  are the minimum and maximum Compton scattering angles that can be measured with the i-TED modules configuration,  $g(\vec{r}; \cos\omega)$  is the projection data in the image space and  $k^{-1}(\vec{r}, \vec{p}; \cos\omega)$  is the inversion kernel. This kernel is defined as

$$k^{-1}(\vec{r}, \vec{p}; \omega) = \sum_{n=0}^{N_{max}} \frac{2n+1}{4\pi H_n} P_n(\cos\omega) P_n(\vec{s} \cdot \vec{r}) \quad (2)$$

with  $H_n$  given by the formula

$$H_n = \int_{\cos\omega_{min}}^{\cos\omega_{max}} \sigma(\cos\omega) P_n^2(\cos\omega) d\cos\omega. \quad (3)$$

In the latter expression  $P_n$  is the Legendre polynomial of order  $n$  and  $\sigma(\cos\omega)$  is the Klein-Nishina Compton differential cross-section<sup>29</sup>.  $N_{max}$  is the maximum number of terms involved in the polynomial expansion and it must be chosen according to the angular resolution of the experimental apparatus, i.e., the experimental angular resolution of the i-TED modules that depends on the selected deposited energy window and the distance between detection planes.

The complexity of this algorithm leads to a large computational cost in order to reconstruct a Compton image with sufficient accuracy. For this reason, the algorithm was implemented in this work for GPU devices using the CUDA toolkit<sup>30</sup>. This methodology allows for a speed-up factor of about  $\sim 121$ , when compared to the singled-threaded CPU version. Additionally, and aiming at quasi-real time image reconstruction in clinical studies,  $H_n$  was pre-computed for a wide range of  $\gamma$ -ray energies and Compton scattering angles corresponding to the range of  $\omega_{min}$  and  $\omega_{max}$  detectable by the i-TED modules. Thus, the  $H_n$  values were saved in a table format for its posterior use, enhancing further the speed of the image reconstruction. More details can be found in Ref.<sup>18</sup>.

The add-back energy-calibrated energy spectrum between detectors of the different i-TED modules during the beam-off period is displayed in Fig. 12. The total add-back spectrum is displayed in blue, while the selected window for the  $\beta^+$  full-energy coincidence peak used for PET imaging is shown by the shadowed red region. The spectra were obtained in time-coincidence between the individual detectors of different i-TED modules using a coincidence time-window of 10 ns. This time window, the same than the one used for the individual i-TED detection planes, was chosen owing to the fast time response of the system and the distance between i-TED modules.

The PET images were reconstructed using a simple analytical algorithm, where straight lines of response (LOR) between the  $\gamma$ -ray interaction positions at the different detectors of the i-TED modules were intersected with the central axial plane. The latter PET imaging plane coincides with the one used for Compton imaging during in the beam-on periods, which was at 85 mm from the front face of the i-TED-A module.

A detailed geometry of the experimental setup was implemented in a C++ Monte Carlo (MC) application based on the GEANT4 toolkit, version 4.10.6<sup>31</sup>. In the MC simulation included the standard electromagnetic package option 3, the radioactive decay, and the packages commonly used in hadron-therapy simulations<sup>32</sup>. These calculations were intended to interpret and cross-check the experimental results obtained for the different configurations, as it is described below in sections , and . A figure of the geometry implemented in the MC code is displayed in Fig. 13. For Compton imaging it includes the two i-TED modules, the sample holder with the samples and the thick graphite layer. For PET imaging the geometry includes also the PLA converter matrix, not shown in Fig. 13. In the simulations, the intrinsic PSD reconstruction resolutions for both position

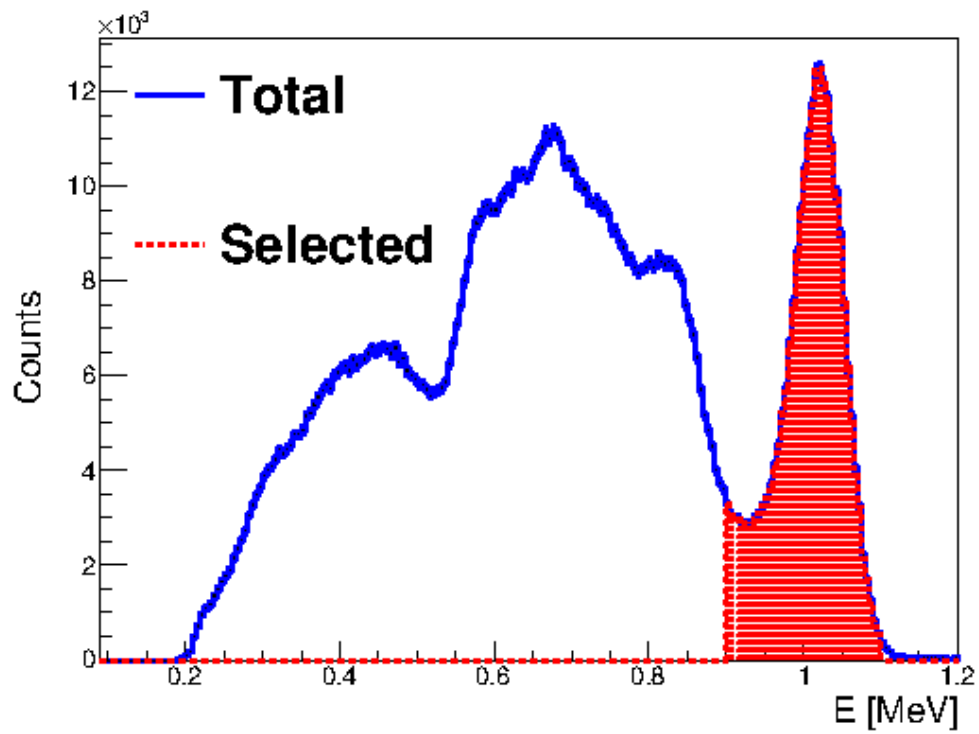


**Figure 12.** Add-back deposited time-coincidence energy spectrum of the i-TED modules during the beam-off period. The selected deposited energy window for PET imaging is displayed by the shadowed red region.

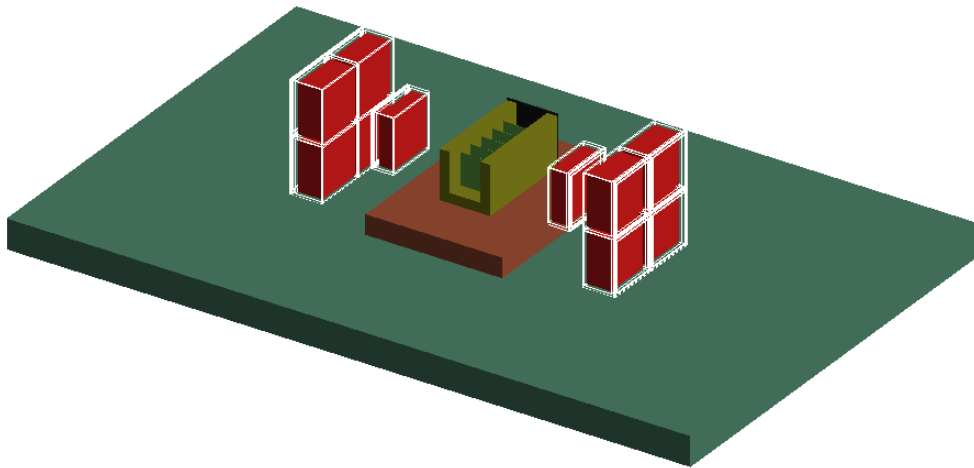


**Figure 13.** Geometry of the experimental setup as implemented in the MC simulation. See text for details.

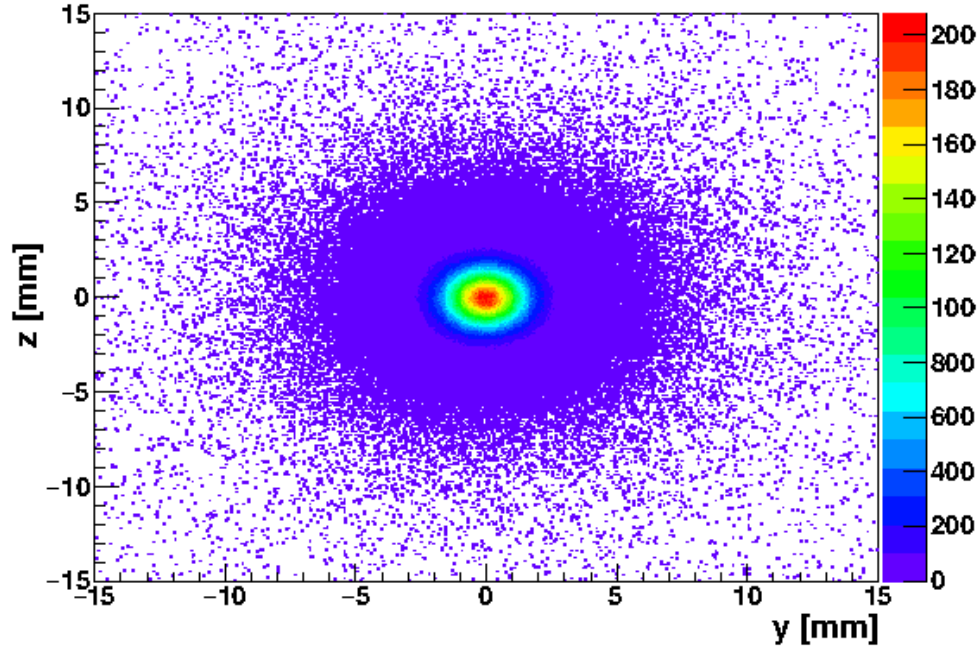


**Figure 14.** Example of MC proton spatial beam profile registered in the thick graphite layer for configuration (I).

and energy-response were included according to the laboratory characterization described in the references<sup>19,33</sup>. The energy dependence of the energy resolution,  $R(E)$ , was determined from the energy calibration procedure using a functional of the form

$$R(E) = \sqrt{a + b/E}, \quad (4)$$

where  $a$  and  $b$  are parameters adjusted from the experimental energy calibrations. For the sake of a realistic comparison, the MC-calculated Compton- and PET-images were reconstructed by implementing exactly the same algorithms and conditions applied to the experimental data.

A further consideration is required regarding the effect of the proton-beam divergence. As protons interact with the sample material along the beam path a spreading is introduced in the transversal spatial profile of the beam. Because the Compton- and PET-imaging algorithms used in this work are based on a single 2D image plane for the reconstruction, the images obtained will reflect also the spreading due to beam straggling effects. In order to account for this experimental effect a dedicated simulation of the proton beam passing through the stack of samples was performed for the three different configurations. This calculation included the different materials and positions in the experimental setup, as shown in Fig. 13. For each simulation study the 3D vertex-positions of the inelastic proton scatterings at the different irradiated layers were registered. As an example, Fig. 14 shows the proton-beam profile calculated at the graphite layer in configuration (I). These distributions will be used afterwards as initial emission-vertex distributions for the PG  $\gamma$ -rays and  $\beta^+$  particles in the beam-on and beam-off modes, respectively. The full-width-at-half-maximum (FWHM) values of the proton beam distribution calculated for the different irradiated layers is displayed in Fig. 15. Configurations (I) and (II) show similar beam spreads at each individual layer for both the Nylon and PMMA material. This was expected because both materials have similar composition and densities. For the configuration (II) the beam profile is much broader due to the effect of the graphite proton-beam degrader just before the sample holder, which increases the width of the incoming proton beam reported in the subsequent sections.

Finally, for the sake of clarity it is worth to indicate that for both, PET and Compton imaging, the reconstruction is made from the reference system or point-of-view of i-TED-B. Thus, the direction of the beam in the images is from the left- to the right-hand side for all the images, being the left-hand side the position of the thick graphite layer and the right hand side the entrance of the proton beam as it schematically shown in panel (a) of Fig. 2.

The above considerations are taken into account in the comparison between simulated and experimental data, which are described for both PET and Compton images in the following sections.

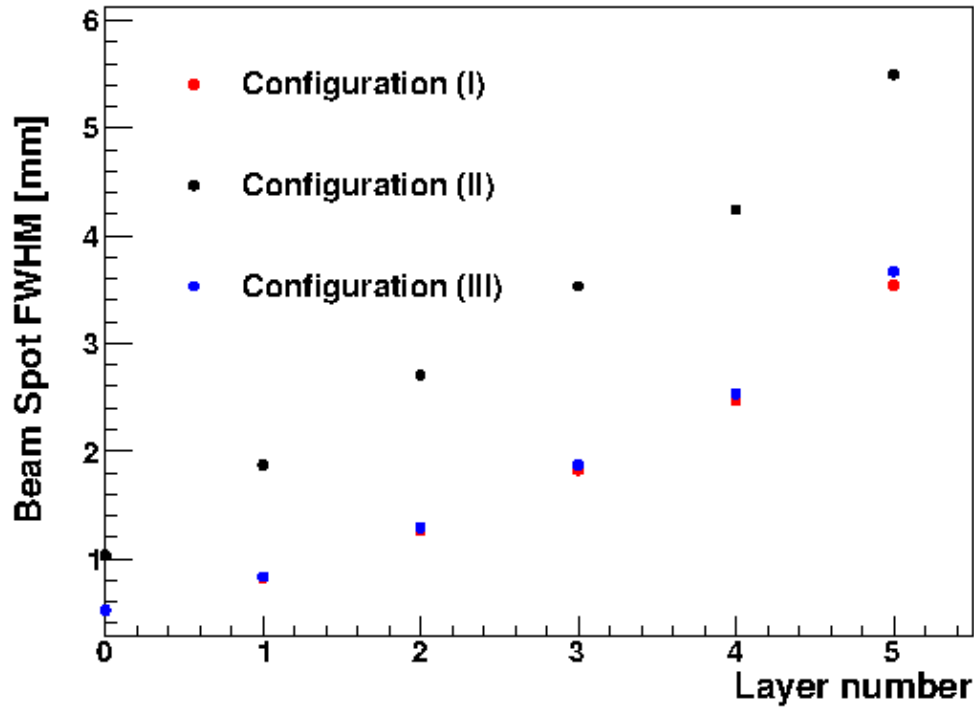


**Figure 15.** MC FWHM of the proton beam spatial distribution at the different layers for the different configurations.

### Laboratory characterization of the i-TED based imaging system

In this section we report on the performance of the two i-TED system for Compton and PET imaging by comparing MC simulations with experimental data for point-like radioactive sources. The goal of this work is to characterize the systematic behaviour of our detection set-up, as a preceding step to the in-beam PET and Compton imaging application.

#### *PET imaging*

The PET performance was experimentally characterized by using a standard point-like  $^{22}\text{Na}$  calibration source placed at the sample-holder slot positions number two, three and four. These positions match with the central region of the imaging system and cover the entire PET field of view between the scatter planes of both i-TED modules. The  $^{22}\text{Na}$  sample was placed at the axial-beam distance, thereby matching well the Compton and PET reconstruction planes.

Projections of the obtained PET distributions along the x- and y-axis for the different slot positions are displayed in Fig. 16 by the red (x) and blue (y) lines, respectively. In the same figure, the black-dashed line shows the MC results from the simulation of the point-like  $^{22}\text{Na}$  source.

A fair agreement is obtained between the experimental results and the MC simulations for all positions. The MC simulations were scaled to match the height of the experimental distributions. In particular, the results for the slot number four are displayed in panel (a) of Fig. 16. The x-coordinate of this position is found to be especially sensitive to pin-cushion effects, since this position is close to the limit of the field-of-view between the scatter planes of both i-TED modules ( $50 \times 50 \text{ mm}^2$ ). The good agreement found between simulation and experiment indicates that pin-cushion effects are properly treated in the reconstructed positions by means of the SVM-method<sup>19</sup>. For the y-axis the agreement between the experimental and MC distributions is also satisfactory. Panel (b) of the same figure shows the results obtained for the  $^{22}\text{Na}$  source in position number three, which corresponds to the geometrical center of the experimental setup. A nice agreement is obtained between the experimental and the MC simulations for both x and y-axis projections, thus validating the intrinsic PSD position-resolution obtained in the previous work<sup>19</sup>. Finally, panel (c) shows the results for the sample-holder position number two, where the situation is comparable to the results obtained for the fourth position.

The PET image resolution for both projection axis are calculated as the FWHM of a Gaussian fit to the experimental data. The results are presented in Tab. 6. As expected, the best resolution in the x-axis is obtained for position number three. As one moves away from this point, slightly broader FWHM values are obtained (positions 2 and 4) reflecting a degradation of the PET resolution. This effect can be explained in terms of the actual intrinsic spatial resolution of the PSDs. As we move from the geometrical center, the time-coincidences ratio between scatter and absorber planes decreases. Therefore, the resolution of the

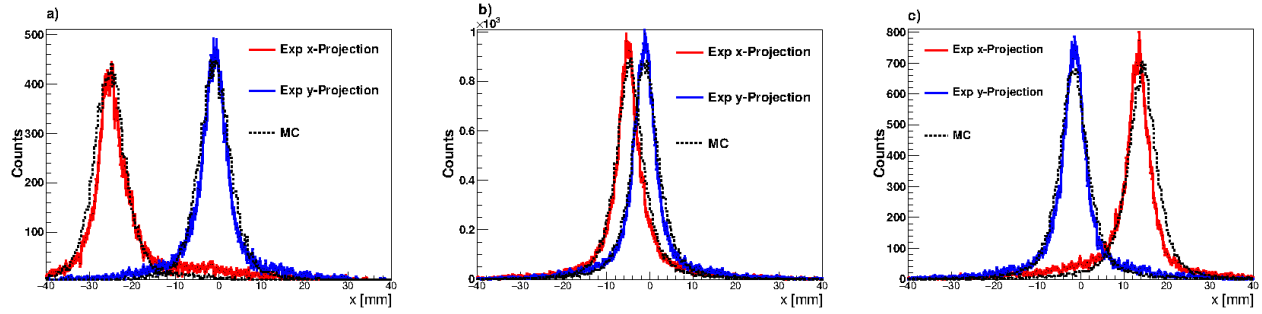


**Figure 16.** x- (red) and y-axis (blue) projections of the PET images for the  $^{22}\text{Na}$  calibration source at different positions along the sample holder. The result of the MC simulation is shown by the dashed-black curve. Panels (a), (b) and (c) correspond to slots number four, three and two in the sample holder.

Position	FWHM x [mm]	FWHM y [mm]
2	6.1(1)	6.2(1)
3	5.6(1)	6.1(1)
4	7.4(1)	6.9(1)

**Table 6.** Experimental x and y-axis FWHM calculated from the experimental  $^{22}\text{Na}$  PET image at the different sample positions.

system will be dominated by the spatial resolution of the thicker absorber detectors<sup>19</sup>.

### Compton imaging

The 2D Compton imaging reconstruction capability and resolution for both i-TED modules was verified by means of a short dedicated measurement with proton beam, where the thick graphite layer was placed in the third position of the sample holder, close to the geometrical center of the experimental setup. The incident beam energy was of 18 MeV. The 2D Compton images independently reconstructed from the measured data for i-TED-A and i-TED-B are displayed in panels (a) and (b) of Fig. 17, respectively. For comparison purposes, a point-like 4.4 MeV source was simulated at the same position. The MC reconstructed images are displayed in panels (c) and (d) for i-TED-A and i-TED-B, respectively. The point-like assumption in the calculation is justified by the fact that the Bragg peak occurs at the very end of the proton track, and therefore the majority of prompt  $\gamma$ -rays are emitted from the same transversal plane along the x- (beam) axis.

A small systematic shift in the x-position was identified after a detailed comparison between the images reconstructed in panels (a) and (b) of Fig. 17. Indeed, the position of the graphite layer is reconstructed with a difference of 10(1) mm between i-TED-A and i-TED-B modules along the x-axis. Since the distance between the detectors was well under control, this shift rather indicates that the central axis of both i-TED modules were not perfectly orthogonal to the beam direction (z-axis). According to the differences in the reconstructed positions and the distance between frontal faces of i-TED modules an angle deviation of about 2-3° with respect to the nominal 90° orientation has been estimated. No attempt has been made to correct for such systematic bias because it does not compromise the imaging results and conclusions of the present work. On the other hand, a more precise and reliable mechanical structure is in preparation for future similar measurements.

Detector	FWHM x [mm]	FWHM y [mm]
i-TED-A	24.73(5)	25.12(3)
i-TED-A (MC)	18.3	18.0
i-TED-B	24.26(6)	24.73(4)
i-TED-B (MC)	19.6	19.4

**Table 7.** Experimental and Monte Carlo FWHM calculated from the Compton images reconstructed using the thick graphite layer in the third position of the samples holder.

The FWHM values obtained for both x- and y-axis projections of the reconstructed Compton images (Fig. 17) are reported in Tab. 7. As expected, the experimental resolutions obtained for both i-TED modules are rather comparable. Compared to the MC point-like  $\gamma$ -ray source simulations, the resolutions obtained experimentally are broad. This might be related to other



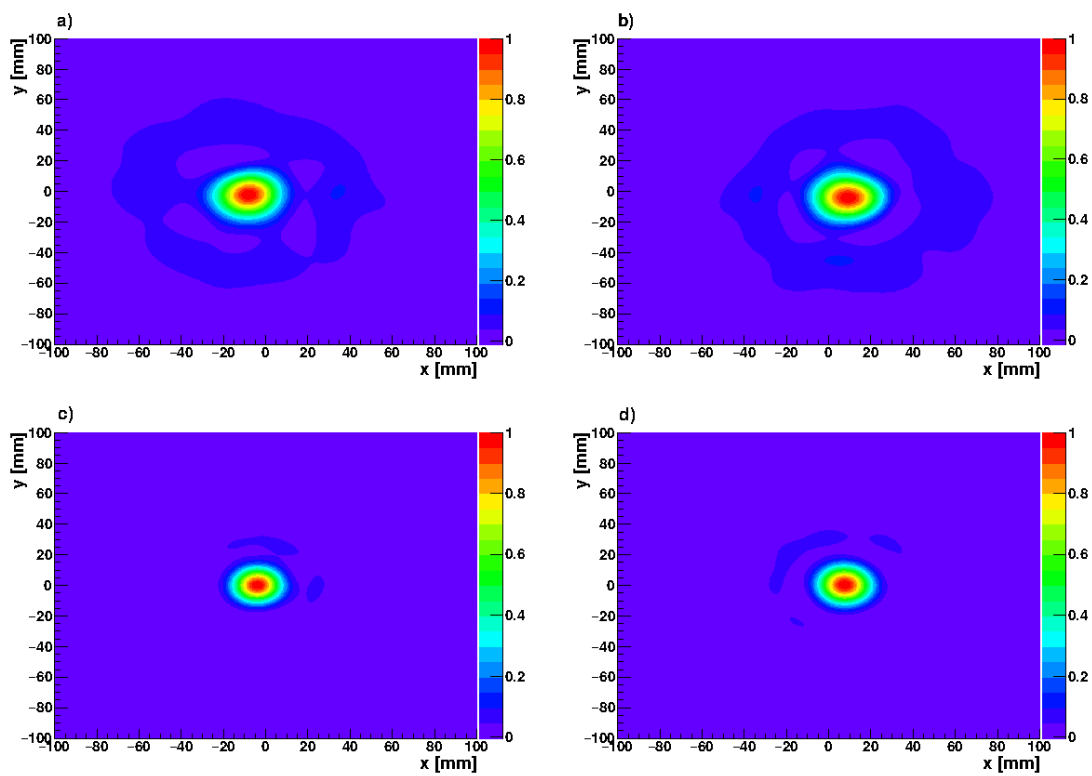


**Figure 17.** Compton images using the 4.4 MeV  $\gamma$ -ray transition from experimental data (top panels a and b) and Monte Carlo simulations (bottom panels c and d) for the thick graphite layer placed at the third slot position of the sample holder irradiated with the proton beam at CNA. See text for details.

systematic uncertainties not accounted as the real PG ray emission distribution, etc.

## References

1. Knopf, A.-C. & Lomax, A. In vivo proton range verification: a review. *Phys. Medicine Biol.* **58**, DOI: [10.1088/0031-9155/58/15/r131](https://doi.org/10.1088/0031-9155/58/15/r131) (2013). <https://doi.org/10.1088/0031-9155/58/15/r131>.
2. Durante, M. & Paganetti, H. Nuclear physics in particle therapy: a review. *Reports on Prog. Phys.* **79**, 096702, DOI: [10.1088/0034-4885/79/9/096702](https://doi.org/10.1088/0034-4885/79/9/096702) (2016).
3. Durante, M., Orecchia, R. & Loeffler, J. S. Charged-particle therapy in cancer: clinical uses and future perspectives. *Nat. Rev. Clin. Oncol.* **14**, 483–495, DOI: [10.1038/nrclinonc.2017.30](https://doi.org/10.1038/nrclinonc.2017.30) (2017).
4. Durante, M. Proton beam therapy in europe: more centres need more research. *Br. J. Cancer* **120**, 777–778, DOI: [10.1038/s41416-018-0329-x](https://doi.org/10.1038/s41416-018-0329-x) (2019).
5. Krimmer, J., Dauvergne, D., Létang, J. & Testa, E. Prompt-gamma monitoring in hadrontherapy: A review. *Nucl. Instruments Methods Phys. Res. Sect. A: Accel. Spectrometers, Detect. Assoc. Equip.* **878**, 58–73, DOI: <https://doi.org/10.1016/j.nima.2017.07.063> (2018). Radiation Imaging Techniques and Applications.
6. Verburg, J. M. & Seco, J. Proton range verification through prompt gamma-ray spectroscopy. *Phys. Medicine Biol.* **59**, 7089–7106, DOI: [10.1088/0031-9155/59/23/7089](https://doi.org/10.1088/0031-9155/59/23/7089) (2014).
7. Parodi, K. & Polf, J. C. In vivo range verification in particle therapy. *Med. Phys.* **45**, e1036–e1050, DOI: <https://doi.org/10.1002/mp.12960> (2018). <https://aapm.onlinelibrary.wiley.com/doi/pdf/10.1002/mp.12960>.
8. Enghardt, W. *et al.* Charged hadron tumour therapy monitoring by means of pet. *Nucl. Instruments Methods Phys. Res. Sect. A: Accel. Spectrometers, Detect. Assoc. Equip.* **525**, 284–288, DOI: <https://doi.org/10.1016/j.nima.2004.03.128> (2004). Proceedings of the International Conference on Imaging Techniques in Subatomic Physics, Astrophysics, Medicine, Biology and Industry.
9. Lopes, P. C. *et al.* First in situ TOF-PET study using digital photon counters for proton range verification. *Phys. Medicine Biol.* **61**, 6203–6230, DOI: [10.1088/0031-9155/61/16/6203](https://doi.org/10.1088/0031-9155/61/16/6203) (2016).
10. Buitenhuis, H. J. T., Diblen, F., Brzezinski, K. W., Brandenburg, S. & Dendooven, P. Beam-on imaging of short-lived positron emitters during proton therapy. *Phys. Medicine Biol.* **62**, 4654–4672, DOI: [10.1088/1361-6560/aa6b8c](https://doi.org/10.1088/1361-6560/aa6b8c) (2017).
11. Tashima, H. *et al.* A single-ring OpenPET enabling PET imaging during radiotherapy. *Phys. Medicine Biol.* **57**, 4705–4718, DOI: [10.1088/0031-9155/57/14/4705](https://doi.org/10.1088/0031-9155/57/14/4705) (2012).
12. Tashima, H. *et al.* Development of a small single-ring OpenPET prototype with a novel transformable architecture. *Phys. Medicine Biol.* **61**, 1795–1809, DOI: [10.1088/0031-9155/61/4/1795](https://doi.org/10.1088/0031-9155/61/4/1795) (2016).
13. Tashima, H. *et al.* 3d Compton image reconstruction method for whole gamma imaging. *Phys. Medicine & Biol.* **65**, 225038, DOI: [10.1088/1361-6560/abb92e](https://doi.org/10.1088/1361-6560/abb92e) (2020).
14. Yoshida, E. *et al.* Whole gamma imaging: a new concept of PET combined with Compton imaging. *Phys. Medicine & Biol.* **65**, 125013, DOI: [10.1088/1361-6560/ab8e89](https://doi.org/10.1088/1361-6560/ab8e89) (2020).
15. Babiano, V. *et al.* First i-TED demonstrator: A Compton imager with Dynamic Electronic Collimation. *Nucl. Instruments Methods Phys. Res. Sect. A: Accel. Spectrometers, Detect. Assoc. Equip.* **953**, 163228, DOI: <https://doi.org/10.1016/j.nima.2019.163228> (2020).
16. Domingo-Pardo, C. i-TED: A novel concept for high-sensitivity (n,  $\gamma$ ) cross-section measurements. *Nucl. Instruments Methods Phys. Res. Sect. A: Accel. Spectrometers, Detect. Assoc. Equip.* **825**, 78 – 86, DOI: <https://doi.org/10.1016/j.nima.2016.04.002> (2016).
17. Pardo, C. D. High-sensitivity Measurements of key stellar Nucleo-Synthesis reactions. <https://hymnserc.ific.uv.es/> (2016). [Online; accessed 13-January-2021].
18. Lerendegui-Marco, J., Balibrea-Correa, J., Babiano-Suárez, V., Ladarescu, I. & Domingo-Pardo, C. Towards machine learning aided real-time range imaging in proton therapy (2022). [2201.13269](https://arxiv.org/abs/2201.13269).
19. Balibrea-Correa, J. *et al.* Machine learning aided 3d-position reconstruction in large LaCl<sub>3</sub> crystals. *Nucl. Instruments Methods Phys. Res. Sect. A: Accel. Spectrometers, Detect. Assoc. Equip.* **1001**, 165249, DOI: <https://doi.org/10.1016/j.nima.2021.165249> (2021).
20. Universidad de Sevilla, C. Centro nacional de aceleradores. <http://cna.us.es/index.php/es/> (2020).

21. Baratto-Roldán, A. *et al.* Preparation of a radiobiology beam line at the 18 mev proton cyclotron facility at cna. *Phys. Medica* **74**, 19–29, DOI: <https://doi.org/10.1016/j.ejmp.2020.04.022> (2020).
22. Baratto-Roldán, A. *et al.* Feasibility study of a proton irradiation facility for radiobiological measurements at an 18 mev cyclotron. *Instruments* **2**, DOI: [10.3390/instruments2040026](https://doi.org/10.3390/instruments2040026) (2018).
23. Rodríguez-González, T. *et al.* Production yields of emitters for range verification in proton therapy. *EPJ Web Conf.* **239**, 24003, DOI: [10.1051/epjconf/202023924003](https://doi.org/10.1051/epjconf/202023924003) (2020).
24. Rodríguez-González, T. *et al.* Production yields at the distal fall-off of the beta+ emitters <sup>11</sup>C and <sup>13</sup>N for in-vivo range verification in proton therapy. *Radiat. Phys. Chem.* **190**, DOI: [10.1016/j.radphyschem.2021.109759](https://doi.org/10.1016/j.radphyschem.2021.109759) (2022).
25. Di Francesco, A. *et al.* TOFPET 2: A high-performance circuit for PET time-of-flight. *Nucl. Instruments Methods Phys. Res. Sect. A: Accel. Spectrometers, Detect. Assoc. Equip.* **824**, 194 – 195, DOI: <https://doi.org/10.1016/j.nima.2015.11.036> (2016). Frontier Detectors for Frontier Physics: Proceedings of the 13th Pisa Meeting on Advanced Detectors.
26. Yap, J., De Franco, A. & Sheehy, S. Future developments in charged particle therapy: Improving beam delivery for efficiency and efficacy. *Front. Oncol.* **11**, DOI: [10.3389/fonc.2021.780025](https://doi.org/10.3389/fonc.2021.780025) (2021).
27. Jolly, S., Owen, H., Schippers, M. & Welsch, C. Technical challenges for flash proton therapy. *Phys. Medica* **78**, 71–82, DOI: <https://doi.org/10.1016/j.ejmp.2020.08.005> (2020).
28. Tomitani, T. & Hirasawa, M. Image reconstruction from limited angle Compton camera data. *Phys. Medicine Biol.* **47**, 2129–2145, DOI: [10.1088/0031-9155/47/12/309](https://doi.org/10.1088/0031-9155/47/12/309) (2002).
29. Klein, O. & Nishina, Y. Über die Streuung von Strahlung durch freie Elektronen nach der neuen relativistischen Quantendynamik von Dirac. *Zeitschrift für Physik* **52**, 853–868, DOI: [10.1007/BF01366453](https://doi.org/10.1007/BF01366453) (1929).
30. Nickolls, J., Buck, I., Garland, M. & Skadron, K. Scalable Parallel Programming with CUDA. *Queue* **6**, 40–53, DOI: [10.1145/1365490.1365500](https://doi.org/10.1145/1365490.1365500) (2008).
31. Allison, J. *et al.* Recent developments in Geant4. *Nucl. Instruments Methods Phys. Res. Sect. A: Accel. Spectrometers, Detect. Assoc. Equip.* **835**, 186 – 225, DOI: <https://doi.org/10.1016/j.nima.2016.06.125> (2016).
32. Verburg, J. M., Shih, H. A. & Seco, J. Simulation of prompt gamma-ray emission during proton radiotherapy. *Phys. Medicine Biol.* **57**, 5459–5472, DOI: [10.1088/0031-9155/57/17/5459](https://doi.org/10.1088/0031-9155/57/17/5459) (2012).
33. Olleros, P. *et al.* On the performance of large monolithic LaCl<sub>3</sub>(Ce) crystals coupled to pixelated silicon photosensors. *J. Instrumentation* **13**, P03014–P03014, DOI: [10.1088/1748-0221/13/03/p03014](https://doi.org/10.1088/1748-0221/13/03/p03014) (2018).

## Acknowledgements

This work has been carried out in the framework of a project funded by the European Research Council (ERC) under the European Union’s Horizon 2020 research and innovation programme (ERC Consolidator Grant project HYMNS, with grant agreement No. 681740). The authors acknowledge support from the Spanish Ministerio de Ciencia e Innovación under grants PID2019-104714GB-C21, FPA2017-83946-C2-1-P, FIS2015-71688-ERC, CSIC for funding PIE-201750I26. This work was partially supported by Generalitat Valenciana PROMETEO/2019/007. We would like to thank the crew at the Electronics Laboratory of IFIC, in particular Manuel Lopez Redondo and Jorge Nácher Arándiga for their excellent and efficient work.

## Author contributions statement

**J.B.C:** Investigation, Methodology, Formal analysis, Software, Data curation, Writing - original draft. **J.L.M:** Investigation, Methodology, Formal analysis, Data curation, Visualization, Writing - review draft. **I.L:** Software, Visualization. **C.D.P:** Conceptualization, Methodology, Investigation, Supervision, Writing - original draft & editing, Funding acquisition. **C.G:** Investigation, Methodology. **T.R.G:** Investigation, Formal analysis. **M.C.J.R:** Investigation, Methodology. **B.F.M:** Investigation.

## Additional information

**Competing interests:** The authors declare that they have no known competing financial interests or personal relationships that could have appeared to influence the work reported in this paper.